Supplementary Information (SI) for Journal of Materials Chemistry C.
This journal is © The Royal Society of Chemistry 2026

Supplementary materials

Flexible RRAM utilizing CdSe Quantum dot-P4VP Composites and Graphene Layer

Boram Kim, ‡[c,e] Jaeyoon Moon, ‡[b] Seonjung Lee,[d,e] Sookyeong Kim,[a,e] Hyungjun Choi,[a,e] Dong-Wook Park, [a,e] Dahin Kim,*[b] and Yoon Kim*[a,e]

[a.] *Department of Electrical and Computer Engineering, University of Seoul, Seoul, 07293, South Korea. E-mail: yoonkim82@uos.ac.kr*
[b.] *Department of Chemical Engineering, Center for Innovative Chemical Processes, Institute of Engineering, University of Seoul, Seoul, 07293, South Korea. E-mail: dhkim23@uos.ac.kr*
[c.] *Institute of Information and Technology, University of Seoul, Seoul, 07293, South Korea.*
[d.] *Department of Intelligent Semiconductor, University of Seoul, Seoul, 07293, South Korea.*
[e.] *Center for Semiconductor Research, University of Seoul, Seoul 02504, South Korea.*

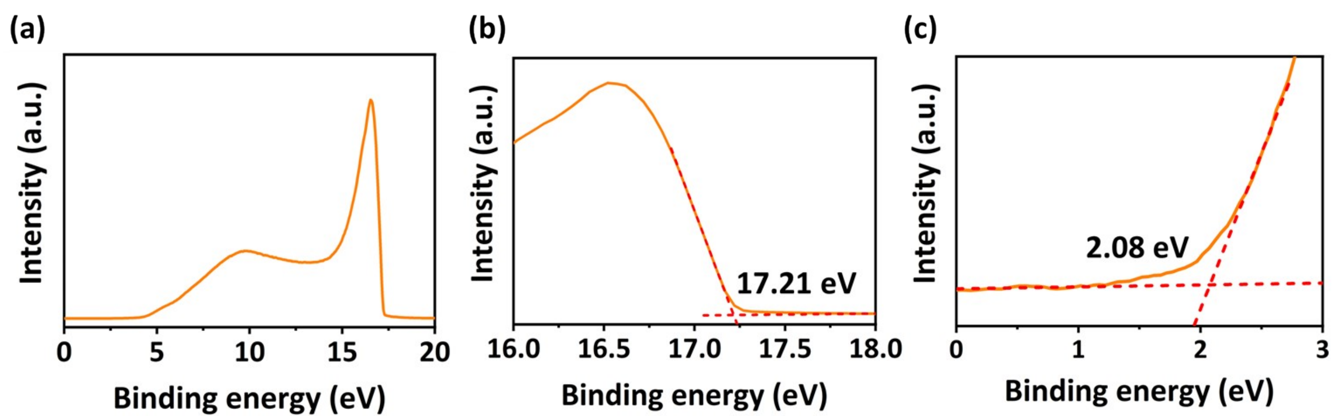

Fig. S1 UV photoelectron spectroscopy (UPS) spectra of CdSe QD. (a) full range, (b) secondary cutoff region, (c) onset region.

Please do not adjust margins

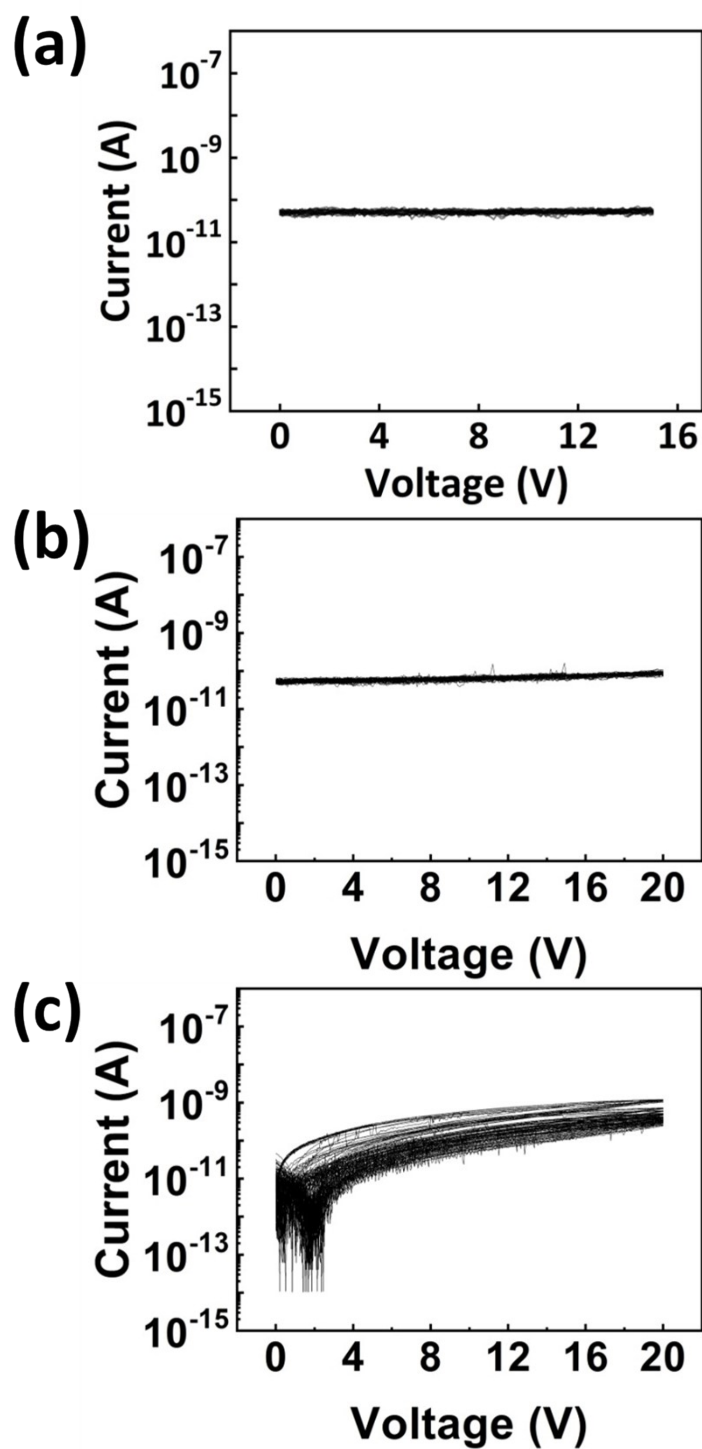

Fig. S2 DC *I-V* characteristics of Al/P4VP/Al devices with varying P4VP concentrations in chloroform. (a) 1 wt%, (b) 3 wt%, (c) 5 wt%.

Please do not adjust margins

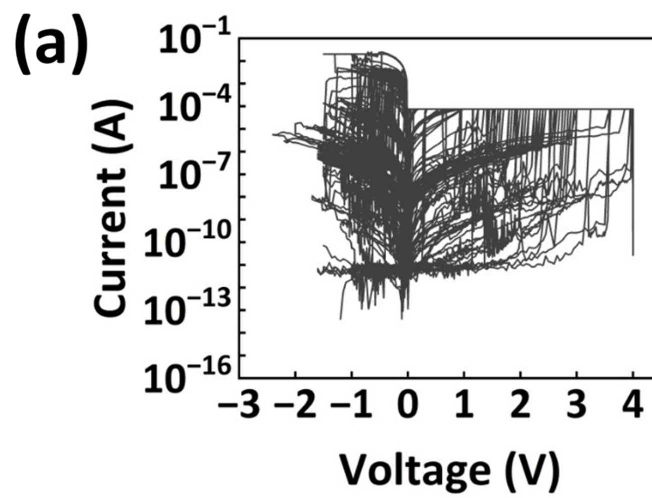

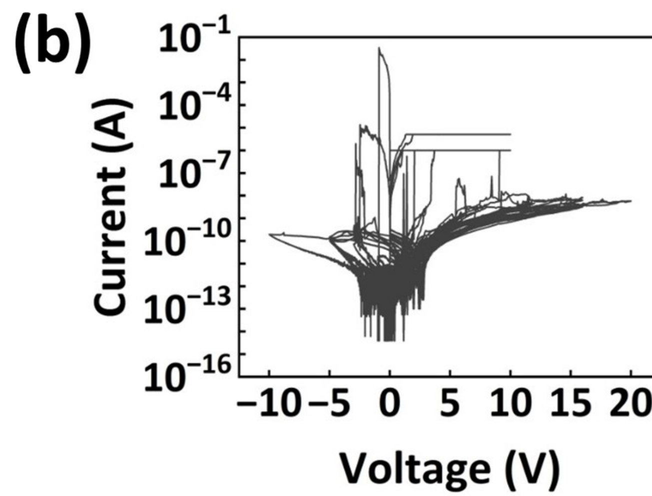

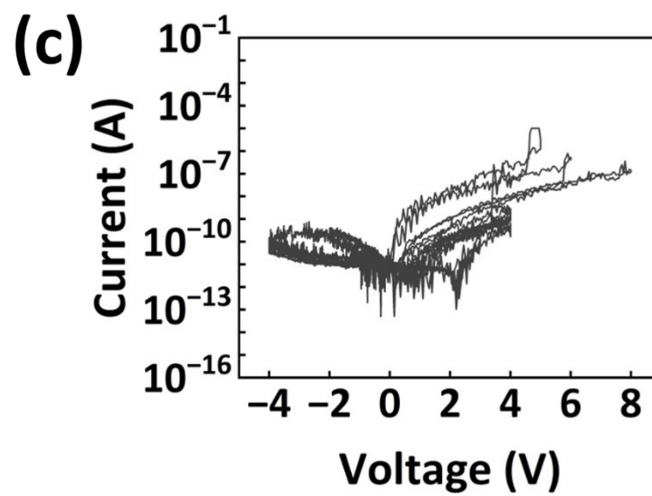

Fig. S3 DC *I-V* characteristics of Al/CdSe QD:P4VP/Al devices with different P4VP concentrations in chloroform. (a) 1 wt%, (b) 3 wt%, (c) 5 wt%.

Please do not adjust margins

TCAD simulation of local electric-field enhancement by CdSe quantum dots

To quantitatively estimate the local electric-field enhancement around CdSe QDs embedded in the P4VP matrix, electrostatic simulations were performed using Sentaurus TCAD. The simulation modelled spherical CdSe QDs (diameter ≈ 3.6 nm, $\varepsilon \approx 9–10$) dispersed within an insulating P4VP matrix ($\varepsilon \approx 3–4$) between Al bottom and top electrodes. As shown in Fig. S4, the simulation reveals pronounced electric-field concentration at the QD–insulator interfaces, particularly for QDs located closer to the top electrode under an applied vertical bias. The maximum electric field reaches 19.58 MV/cm, which is significantly higher than that of the QD-free structure under identical conditions. This localized field amplification arises from the dielectric mismatch between CdSe and P4VP, which causes the QDs to act as nanoscale field concentrators via Maxwell–Wagner–Sillars interfacial polarization. The resulting enhanced local field promotes Al-ion oxidation at the anode and accelerates ion drift into the active layer, thereby facilitating the nucleation of QD-centred hybrid conductive filaments.

This journal is © The Royal Society of Chemistry 20xx

Please do not adjust margins

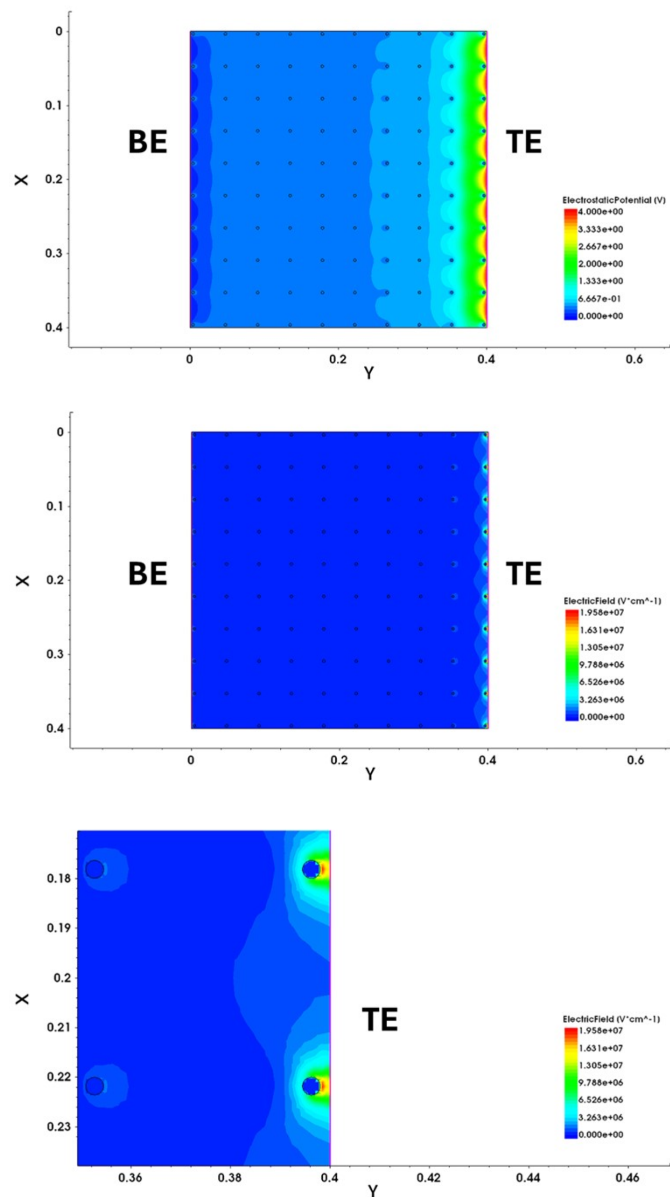

Fig. S4 Electric-field distribution obtained from Sentaurus TCAD simulation illustrating the field-concentration effect induced by CdSe quantum dots (QDs) embedded in the insulating layer between the bottom electrode (BE) and the top electrode (TE). The maximum electric field reaches 19.58 MV/cm at the QD–insulator interfaces under an applied vertical bias.

Please do not adjust margins

Quantitative trap density analysis from SCLC fitting

To validate the trap-assisted transport mechanism inferred from the log–log I–V analysis, the trap density (N_t) was systematically extracted across 87 graphene-integrated devices comprising 3,263 valid switching cycles. For each cycle, the trap-filled limit voltage (V_{TFL}) was identified as the transition point where the local log–log slope exceeds 4, marking the onset of the trap-filled space-charge-limited conduction regime. The trap density was then calculated using $N_t = 2\varepsilon_0\varepsilon_r V_{TFL} / (qd^2)$, where $\varepsilon_r = 4$ is the relative permittivity of the CdSe QD–P4VP composite and d = 380 nm is the active layer thickness.

As shown in Fig. S5(a), the cycle-wise N_t distribution remains consistently within the 10^{14}–10^{16} cm^{-3} range for both SET and RESET operations, with median values of 3.5×10^{15} cm^{-3} (SET) and 2.1×10^{15} cm^{-3} (RESET). To exclude the influence of extreme cycles, trimmed statistics were applied by removing the minimum and maximum values per device prior to averaging. The resulting device-level trimmed mean trap densities, shown in Fig. S5(b), demonstrate stable and reproducible N_t values across 70 (SET) and 60 (RESET) devices, confirming that the extracted trap density represents an intrinsic property of the CdSe QD–P4VP composite rather than cycle-to-cycle artefacts. Fig. S5(c) presents box plots of the extracted log–log slopes for the three conduction regimes (Ohmic, trap-controlled SCLC, and trap-filled SCLC), with median and interquartile range (IQR) statistics confirming reproducible slope distributions characteristic of each transport regime.

This journal is © The Royal Society of Chemistry 20xx

Please do not adjust margins

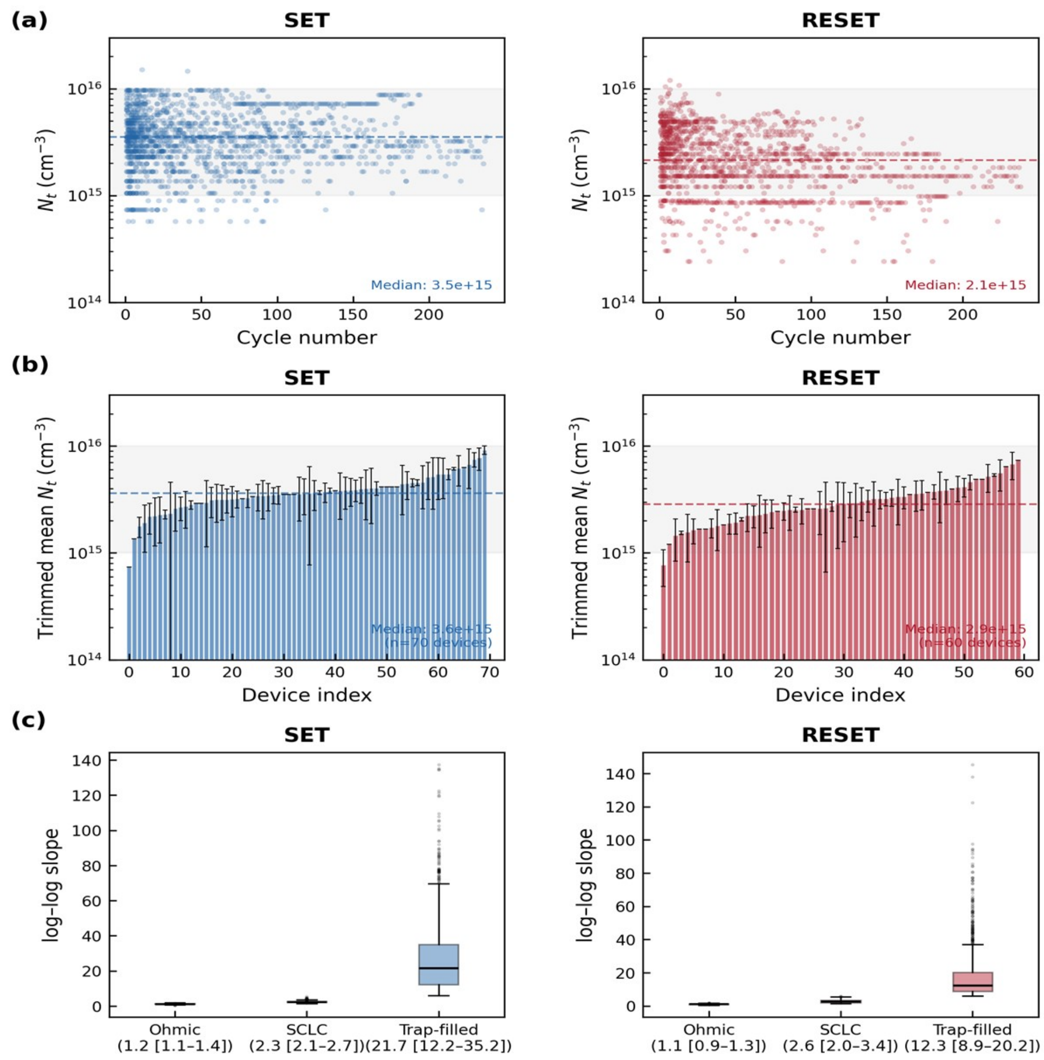

Fig. S5 Quantitative validation of trap-assisted transport across 87 graphene-integrated devices (3,263 valid switching cycles). (a) Cycle-wise trap density (N_t) distribution for SET and RESET operations. Dashed lines indicate medians. The grey shaded band marks the 10^{15}–10^{16} cm^{-3} range. (b) Device-level trimmed mean N_t. (c) Box plots of extracted log–log slopes for the three conduction regimes. Boxes show median and IQR; whiskers extend to 1.5 × IQR.

Please do not adjust margins

Compositional analysis of the conductive filament across resistive states

To directly confirm the composition of the conductive filament, cross-sectional TEM imaging and EDS elemental mapping were performed on the Al/Graphene/P4VP:CdSe QD/Al device under three resistive states. In the pristine state (Fig. S6(a)), a uniform elemental distribution is observed without Al penetration into the active layer. After SET switching into the LRS (Fig. S6(b)), the EDS mapping reveals the presence of Al species concentrated within the switching region, confirming the formation of metallic Al-based conductive filaments. Following RESET to the HRS (Fig. S6(c)), the Al distribution returns toward the pristine configuration, consistent with filament rupture. These results, together with previous literature on Al-driven conductive-bridge mechanisms, strongly indicate that the dominant filament component is metallic Al rather than carbonised polymer pathways or QD-mediated hopping conduction.

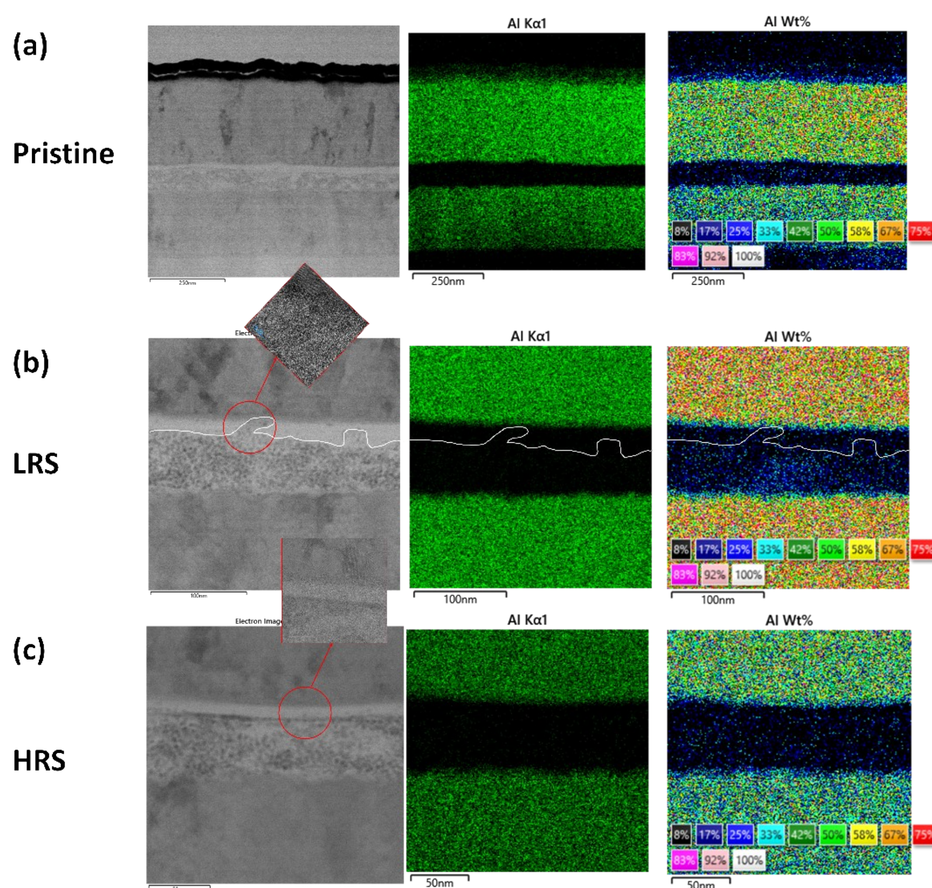

Fig. S6 Cross-sectional TEM images and EDS elemental mapping of the Al/Graphene/P4VP:CdSe QD/Al device under three resistive states: (a) pristine (as-fabricated), (b) low-resistance state (LRS, after SET), and (c) high-resistance state (HRS, after RESET).

This journal is © The Royal Society of Chemistry 20xx

Please do not adjust margins

Characterisation of the transferred CVD graphene

The structural quality and electrical continuity of the transferred CVD graphene were characterised by Raman spectroscopy and sheet resistance measurements. As shown in Fig. S7, the Raman spectrum exhibits the characteristic D, G, and 2D peaks, with a measured D/G intensity ratio of 0.3693. This value indicates the presence of moderate structural defects typically observed in transferred CVD graphene, while remaining within the commonly reported range for large-area CVD graphene. This level of defect density is sufficient for maintaining the high in-plane electrical and thermal transport properties required for the device functionality.

The sheet resistance was measured at multiple positions across the sample using silver paste contacts (Fig. S8). The extracted values range from approximately 199 to 242 Ω/sq, with an average of ~209 Ω/sq and a standard deviation of ~9 Ω (coefficient of variation ≈ 4–5%). This small spatial variation confirms good electrical uniformity and film continuity over the measured area. Continuity information provided by the supplier further confirms uniform monolayer coverage across the substrate without macroscopic cracks or discontinuities.

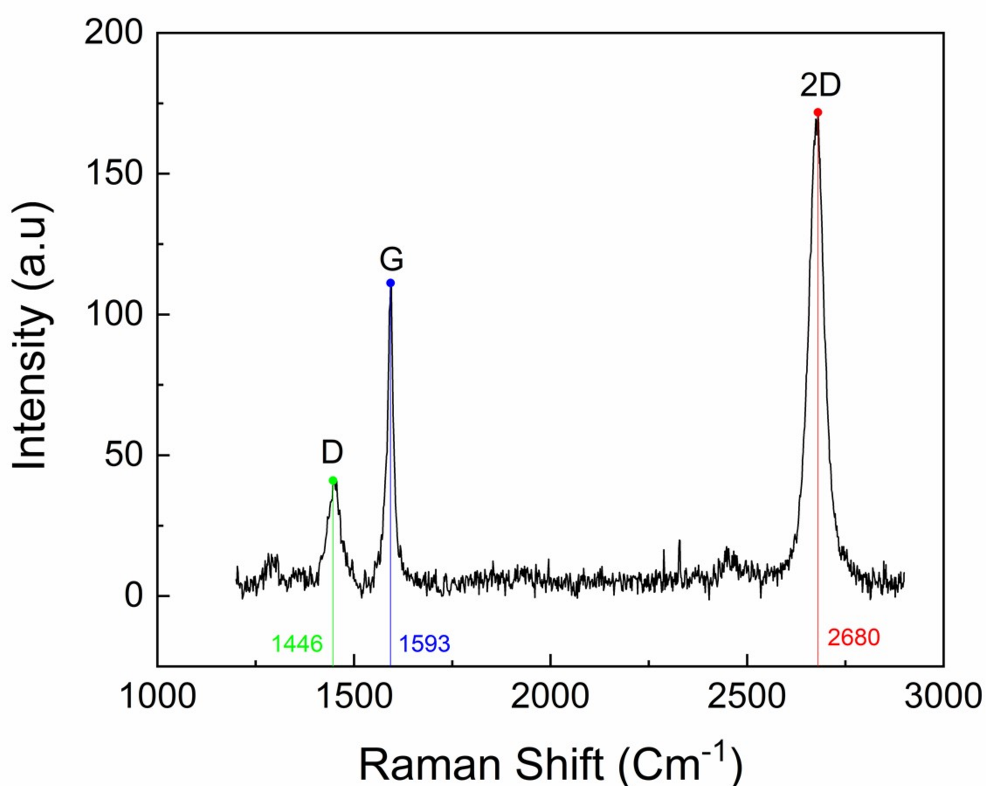

Fig. S7 Raman spectroscopy of the transferred CVD graphene. The measured D/G intensity ratio is 0.3693.

Please do not adjust margins

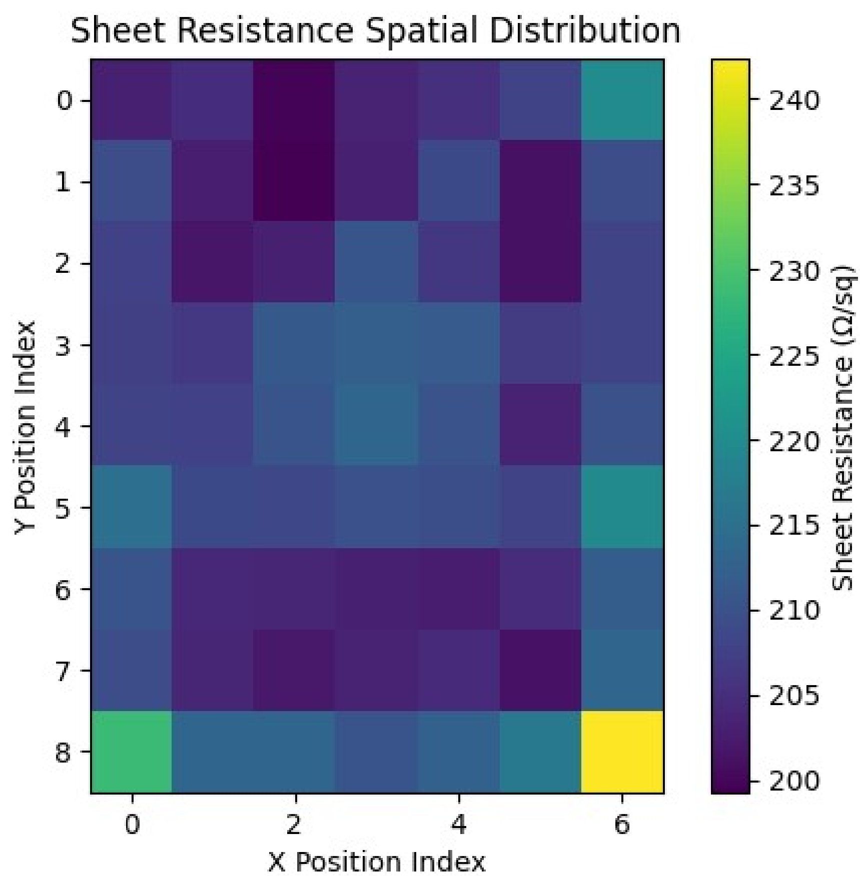

Fig. S8 Sheet resistance measured at multiple positions across the transferred graphene sample. Values range from approximately 199 to 242 Ω/sq (average ~209 Ω/sq, CV ≈ 4–5%).

Please do not adjust margins

Monte Carlo analysis of neuromorphic inference accuracy under device variability

To assess the sensitivity of the MNIST classification accuracy to realistic device variability, a systematic Monte Carlo analysis was performed (N = 30 independent trials per condition) under two variability models. Cycle-to-cycle read noise was modelled as $\sigma = \alpha \cdot G$, where α equals the coefficient of variation (CV) directly. As summarised in Table S1, both Identical and ISPP schemes degrade gracefully with increasing read noise. At α = 2%, a representative value for typical oxide RRAM, Identical retains 88.59 ± 0.12% and ISPP retains 89.12 ± 0.10%, representing a degradation of less than 0.2 pp from the noiseless baseline. This moderate sensitivity arises because the differential-pair architecture ($\Delta W = G^{+} - G^{-}$) provides inherent common-mode noise rejection.

Table S1. MNIST accuracy vs. read-noise CV α (D2D variation off, N = 30 MC trials).

α (CV, %)	Identical Mean ± SD (%)	Identical Q05 (%)	ISPP Mean ± SD (%)	ISPP Q05 (%)	Δ ISPP − Identical (pp)
0	88.72 ± 0.00	88.72	89.35 ± 0.00	89.35	+0.63
1	88.70 ± 0.09	88.55	89.28 ± 0.06	89.19	+0.59
2	88.59 ± 0.12	88.43	89.12 ± 0.10	89.00	+0.53
5	87.83 ± 0.24	87.34	88.27 ± 0.19	87.93	+0.44
10	85.11 ± 0.40	84.49	85.33 ± 0.47	84.57	+0.21
25*	69.54 ± 1.04	67.59	70.89 ± 1.34	68.97	+1.35

* α = 25% represents a physically extreme noise level included to characterise graceful degradation behaviour.

To account for realistic deployment conditions, a second sweep was conducted incorporating device-to-device (D2D) lognormal variation with parameters derived from the experimental device statistics: HRS D2D CV = 25%, LRS D2D CV = 10%, and an additional low-conductance tail correction of CV = 15% applied to the bottom 15th percentile of HRS devices. As shown in Table S2, D2D variation is the dominant accuracy-limiting mechanism. With D2D variation only (α = 0), Identical yields 81.37 ± 1.82% and ISPP yields 84.25 ± 1.21%. The ISPP advantage expands from +0.63 pp in the read-noise-only regime to +2.88 pp in mean accuracy and +4.54 pp on the worst-case Q05 metric (Identical Q05 = 77.72% vs. ISPP Q05 = 82.26%), attributable to ISPP's iterative pulse-verify programming that confines each programmed conductance within a target window.

Table S2. MNIST accuracy under combined D2D lognormal variation and read noise (CV_HRS = 0.25, CV_LRS = 0.10, low-G extra CV = 0.15; N = 30 MC trials).

Condition	Identical Mean ± SD (%)	Identical Q05 (%)	ISPP Mean ± SD (%)	ISPP Q05 (%)	Δ ISPP − Identical (pp)
D2D only (α = 0%)	81.37 ± 1.82	77.72	84.25 ± 1.21	82.26	+2.88
D2D + α = 1%	81.36 ± 1.78	77.75	84.21 ± 1.21	82.20	+2.85
D2D + α = 2%	81.26 ± 1.77	77.74	84.06 ± 1.21	81.99	+2.80
D2D + α = 5%	80.57 ± 1.74	77.38	83.27 ± 1.20	81.00	+2.70
D2D + α = 10%	78.23 ± 1.69	75.59	80.64 ± 1.22	78.24	+2.41

Please do not adjust margins

The baseline accuracy values in Table S1 (Identical: 88.72%, ISPP: 89.35%) differ from the main-text values (IDP: 73.98%, ISPP: 87.41%) because the two simulation frameworks serve different purposes. The main-text accuracy is derived from on-chip learning using the experimentally fitted conductance update curves, which reflect the full training dynamics including nonlinearity and asymmetry of the weight update function. In contrast, the Monte Carlo variability analysis uses the experimentally extracted discrete conductance levels with an ideal weight mapping, in order to isolate the effect of device variability from the training algorithm. Both frameworks use the same 784×10 single-layer network and binarised MNIST dataset.

Thermal estimation for the graphene interlayer

Although graphene is atomically thin, it possesses exceptionally high in-plane thermal conductivity. Previous experimental studies have reported that supported CVD graphene exhibits a thermal conductivity of approximately 300–600 W m^{-1} K^{-1} (ref. 34), which is more than three orders of magnitude higher than that of typical polymer matrices (~0.2 W m^{-1} K^{-1}). Graphene therefore primarily acts as an in-plane heat-spreading layer rather than a volumetric heat buffer. Under a typical SET pulse condition (I ≈ 10 μA, V ≈ 2 V), the Joule heating power is approximately 20 μW, localised within a nanoscale filament region. The thermal diffusivity of graphene ($\alpha = k/\rho c$) is on the order of 10^{-4} m^2 s^{-1}. For a pulse duration of 100 ns, the thermal diffusion length can be estimated as $L_{th} = \sqrt{\alpha t}$ ≈ several micrometres, which is orders of magnitude larger than the filament diameter (~10–20 nm). This indicates that graphene can laterally redistribute heat over a micrometre-scale region within the pulse duration, thereby reducing local temperature accumulation and stabilising filament formation.

Mechanical analysis of the flexible device under bending

The device was fabricated on a 10 μm-thick freestanding Parylene-C substrate. Under a bending radius of 5 mm, the maximum surface strain can be estimated using $\varepsilon_{max} = t/2R$, yielding approximately 0.11%. Given that the Parylene substrate dominates the total thickness of the multilayer stack, the neutral mechanical plane is expected to lie near the mid-plane of the 10 μm substrate. Consequently, the QD:P4VP active layer, located close to the substrate surface, experiences a strain on the order of 0.1%, which is relatively small for polymer-supported thin-film devices.

With respect to strain-induced band modulation in CdSe quantum dots, deformation potential theory indicates that sub-percent elastic strain results in band-edge shifts in the meV range for direct bandgap semiconductors such as CdSe. At an estimated strain level of ~0.1%, the expected band shift is limited to only a few meV, which is negligible compared to the volt-level electric fields involved in filament formation and ion migration. Similarly, flexoelectric polarisation arises from strain gradients rather than uniform strain. Under a bending radius of 5 mm, the strain gradient across the ~380 nm active layer is very small (on the order of 1/R), suggesting that any flexoelectric contribution would be weak.

Synaptic update energy estimation under ISPP conditions

Under ISPP conditions (70 μs pulse width), the synaptic update energy for both SET and RESET operations was estimated using the relation $E = G \cdot V^2 \cdot \tau$, where G is the conductance after each incremental step, V is the applied

This journal is © The Royal Society of Chemistry 20xx

Please do not adjust margins

programming voltage, and τ is the pulse duration. The average energy per programming pulse was approximately 4 nJ for SET and 1.8 nJ for RESET. When considering a full ISPP sequence of ≈46 incremental SET steps and ≈48 RESET steps, the cumulative update energy per programming event was approximately 180 nJ (SET) and 86 nJ (RESET). These values are consistent with polymer/organic synaptic memory systems (refs. 37, 38) operating with 70 µs programming pulses and relatively high conductance levels. The higher energy per event compared to oxide RRAM (refs. 35, 36) arises principally from the longer pulse duration and increased programming currents characteristic of the QD–polymer composite, reflecting a trade-off between gradual incremental programming and energy efficiency.